

AVA and AVAZ of 3D pre-stack seismic data in Altamont-Bluebell field

Khaled Al Dulaijan and Gary F. Margrave

ABSTRACT

In this paper, the Altamont-Bluebell 3D pre-stack seismic data is analyzed using AVA to identify sweet spots and using AVAZ to identify azimuthal seismic anisotropy zones and correlate them to sweet spots. In AVA analysis, the reflection coefficient is a function of incident angle and the three elastic parameters or P-wave velocity, S-wave velocity, and density. Therefore, those parameters are inverted for. In AVAZ analysis, four additional quantities (the symmetry angle and the three TI symmetry parameters) need to be obtained by inversion of the azimuth/angle-dependent reflection coefficient. Since the reflection coefficient in the AVAZ case is a higher-order function of seven parameters, we may require include information from larger incident angles as compared to AVA analysis. This will be discussed here. The geology of the field, and seismic data acquisition were described earlier in Al Dulaijan (2017). Our focus will be on the main two targets. The first target is the most prolific oil interval within the overpressured Wasatch. This interval is about 500' thick, and called Wasatch 180. Most horizontal wells are drilled within this target. The second target is the shallower and thicker gas reservoir within the Upper Green River (UGR) formation.

SEISMIC DATA PROCESSING FOR AVA & AVAZ

A conventional 3D processing workflow was applied to the Altamont-Bluebell data. After geometry assignment, an amplitude recovery function of velocity was applied. Refraction statics were applied too with a replacement velocity of 8000 ft/sec and two-layer model. The offsets used were about 250 to 2000 feet for the first layer, and about 2100 to 7000 feet for the second layer. Figure 1, Figure 2, and Figure 3 show the elevation, elevation statics, and refraction statics of sources and receivers. For definitions of those statics and more about refraction statics, please refer to Al Dulaijan (2008). Heavy noise were observed and suppressed in multiple domains (i.e., shot, CDP, inline-azimuth-shot line). Also, spherical divergence correction, surface-consistent amplitude corrections, and deconvolution were applied. The zero-offset VSP data were used to calculate Q corrections for the 3D seismic data, and also to determine phase corrections for bringing the surface seismic data to zero phase. Isotropic velocity analysis at one-mile intervals, NMO corrections, and residual statics corrections (for common-azimuth varying-offset gathers) were done in sequence. A second pass of velocity analysis at half-mile intervals was done, followed by another pass of residual statics corrections and by a second pass of surface-consistent amplitude processing.

In standard industry practice, azimuthal variations are usually preserved either by sectoring prestack data into azimuthal sectors, or by COV binning. The latter has the advantage of preserving more azimuthal variations. COV sorting is described by Carey

(1999); Li (2008) gives a detailed explanation of the method. COV binning of the data prior to migration was chosen here.

Then, isotropic migration velocity analysis was preformed, and followed by anisotropic VTI migration velocity analysis. VTI COV Kirchhoff prestack time migration (PSTM) was carried on for at last. PSTM gather is shown by Figure 4. Trim statics processing was applied to flatten target horizons for both AVA and AVAZ data. For AVA inversion, a super gather was created from 9 gathers. For AVAZ inversion, 9 non-stacked gathers were used for each CDP location.

PSTM gathers were stacked. Stacked data were correlated to well logs and used to pick horizons. Figure 5 shows inline and crossline stack sections with a well in the middle and two picked horizons, Upper Green River formation and Mahogany Bench which are the top and base of the shallow target. An example logs for one of the available wells are shown by Figure 7. The original logs are shown indicated by grey curves. Those logs were temporally filtered to 100 Hz. Filtered logs are indicated by black curves. The base of Lower Green River is the marker for Wasatch that starts at depth of 12380'. The first target which the most prolific zone of Wasatch starts at 13750' and is about 500' thick. Even though Wasatch is overpressured as indicated by low P-wave velocities, the productive zone (Wasatch-180) is not, according to high P-wave velocity logs for this well and other available well. The reason may be due to the fact that the reservoir has been producing for long and is in depleting stage now. Hydrocarbon generation in the low-permeability and low-porosity Flagstaff is the reason for the overpressure in Wasatch (Morgan et. al, 2003). For the shallower target, Upper Green River formation, the only available log here is P-wave sonic. The porosity of Wasatch 180 is low. For all wells, Lower Green River formation showed the highest porosity. However, high porosity at Lower Green River in Altamont- Bluebell field do not translate into high oil production (Morgan et al., 2003). Well logs are correlated to seismic and used to pick the top and base of those two targets. The time picks for Upper Green River formation and Mahoney Bench are displayed in Figure 8. Isochrone or time thickness of this Upper Green River is displayed in Figure 9. Thickness of this reservoir does not vary significantly. Figure 10 shows time picks of Wasatch 180 and its base, and Figure 11 shows an isochrone of the reservoir. Wasatch-180 thins toward the North.

Angles of incidence were calculated from the ray parameter (p) (CGGVeritas, 2014):

$$p = \frac{\sin \theta}{V_{int}}, \quad (1)$$

where V_{int} is the isotropic interval P-wave velocity. The ray parameter (p) can also be calculated by taking the derivative of V_{rms} (i.e., RMS velocity from the NMO equation) with respect to the offset coordinate (x):

$$t_x^2 = t_0^2 + \frac{x^2}{V_{rms}^2}, \quad (1)$$

$$p = \frac{dt}{dx}, \quad (2)$$

$$\frac{dt}{dx} = \frac{x}{t_x V_{rms}^2}. \quad (3)$$

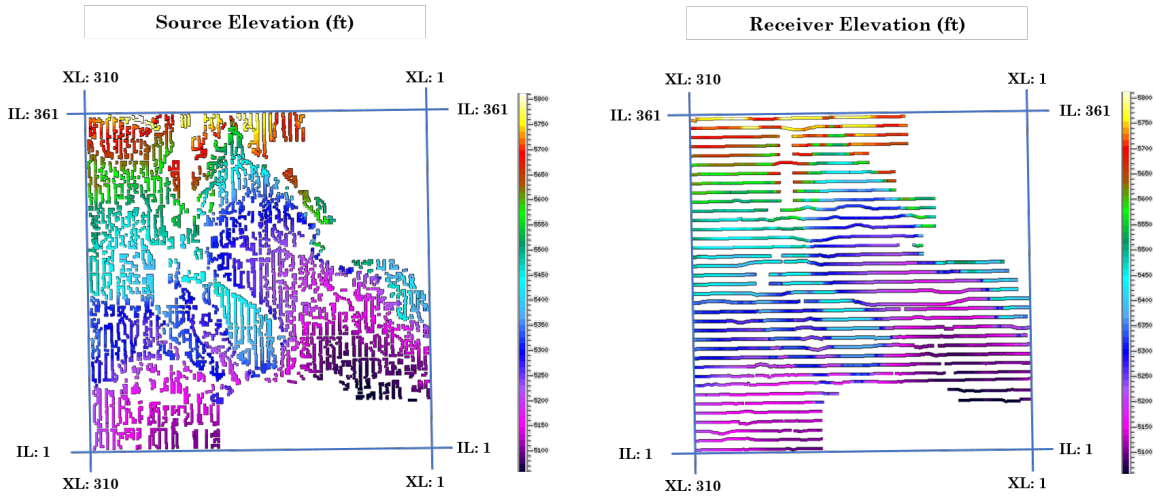


Figure 1 Elevation basemap of sources (left) and receivers (right). Elevation increases toward north and has about 800-ft range.

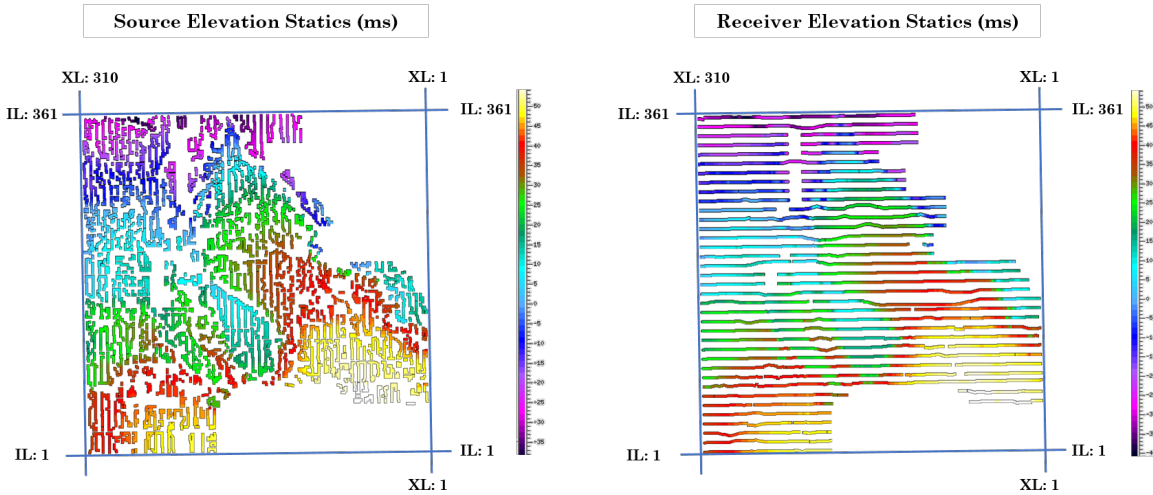


Figure 2 Elevation statics basemap of sources (left) and receivers (right).

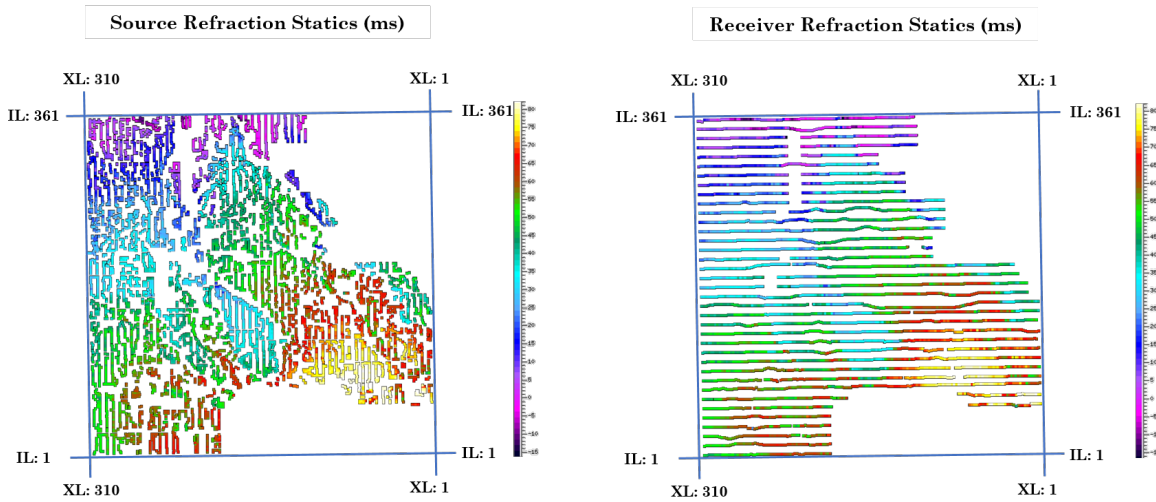


Figure 3 Refraction statics basemap of sources (left) and receivers (right).

Rewriting Equation (14) yields

$$\sin \theta = \frac{x Vint}{t_x Vrms^2}. \quad (4)$$

From the geometry of source-receiver pair in a single constant velocity layer shown in Figure 6:

$$t_x = \frac{t_0}{\cos \theta}. \quad (5)$$

For a single layer $Vint$ and $Vrms$ are equal, therefore substituting t_x from Equation (6) into Equation (5) yields:

$$\tan \theta = \frac{x}{t_0 Vint}. \quad (6)$$

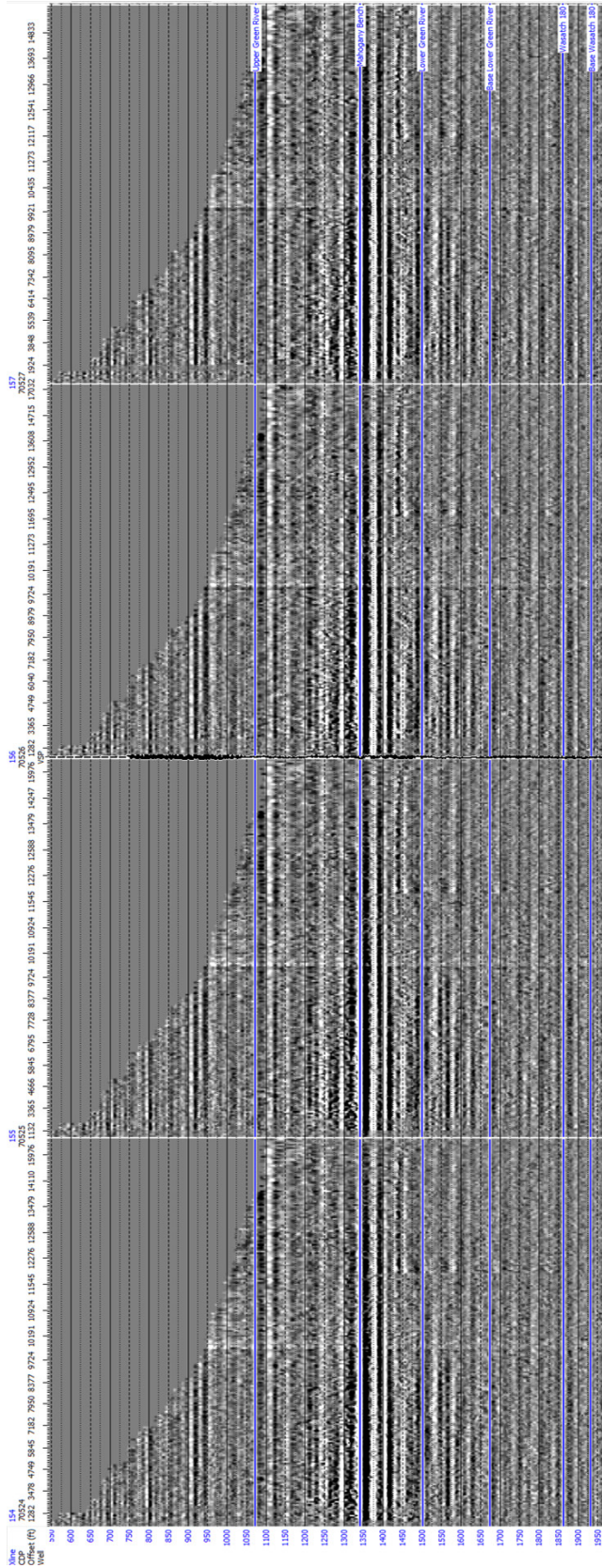


Figure 4 PSTM Gathers close to the VSP borehole. Five horizons are picked and shown by blue.

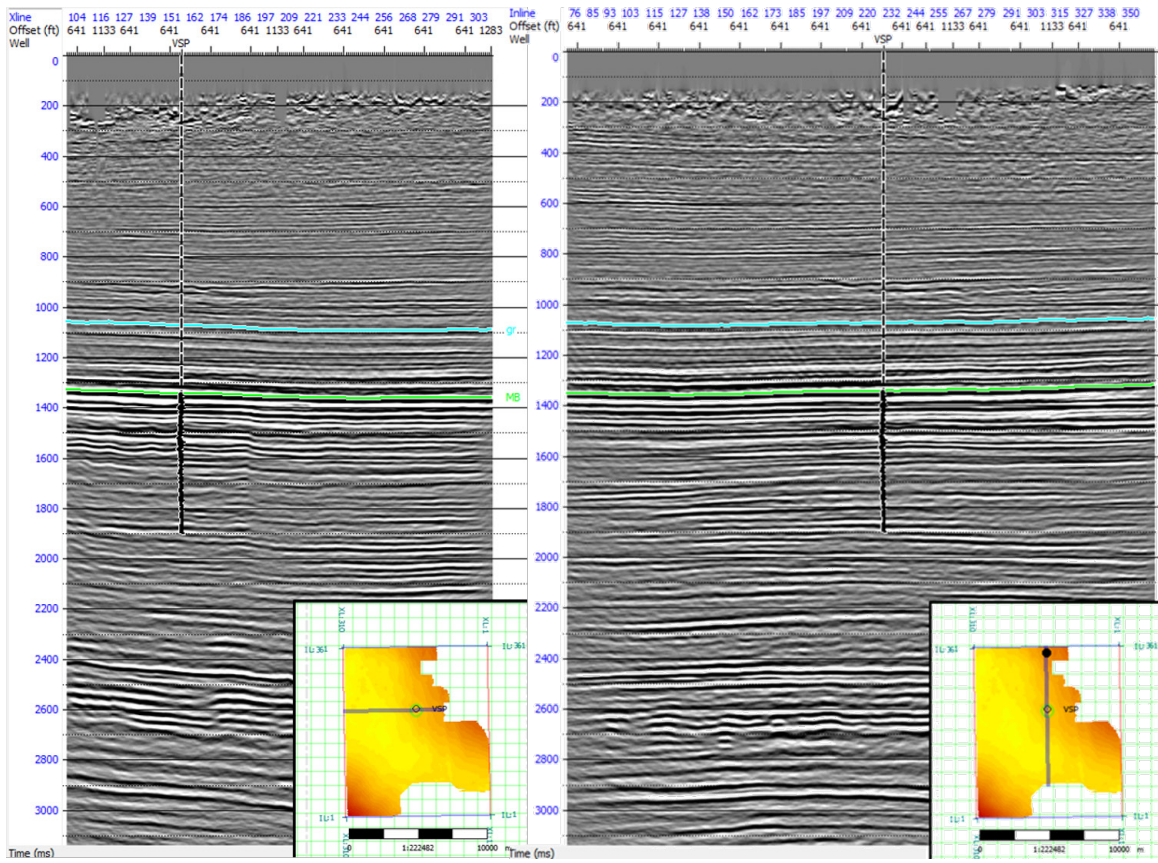


Figure 5 PSTM stacked inline (left) and cross line (right) with basemaps and relative stacked section location on bottom rights.

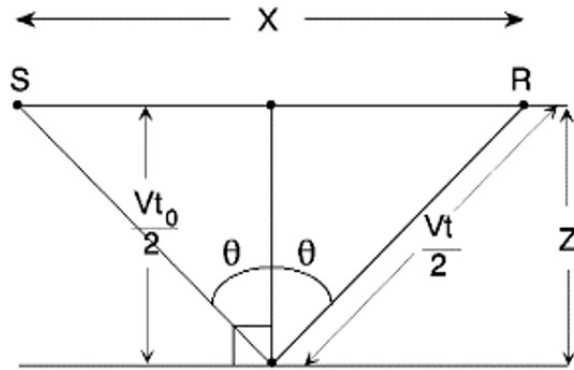


Figure 6 Raypath of a source-receiver pair in a single constant velocity layer.

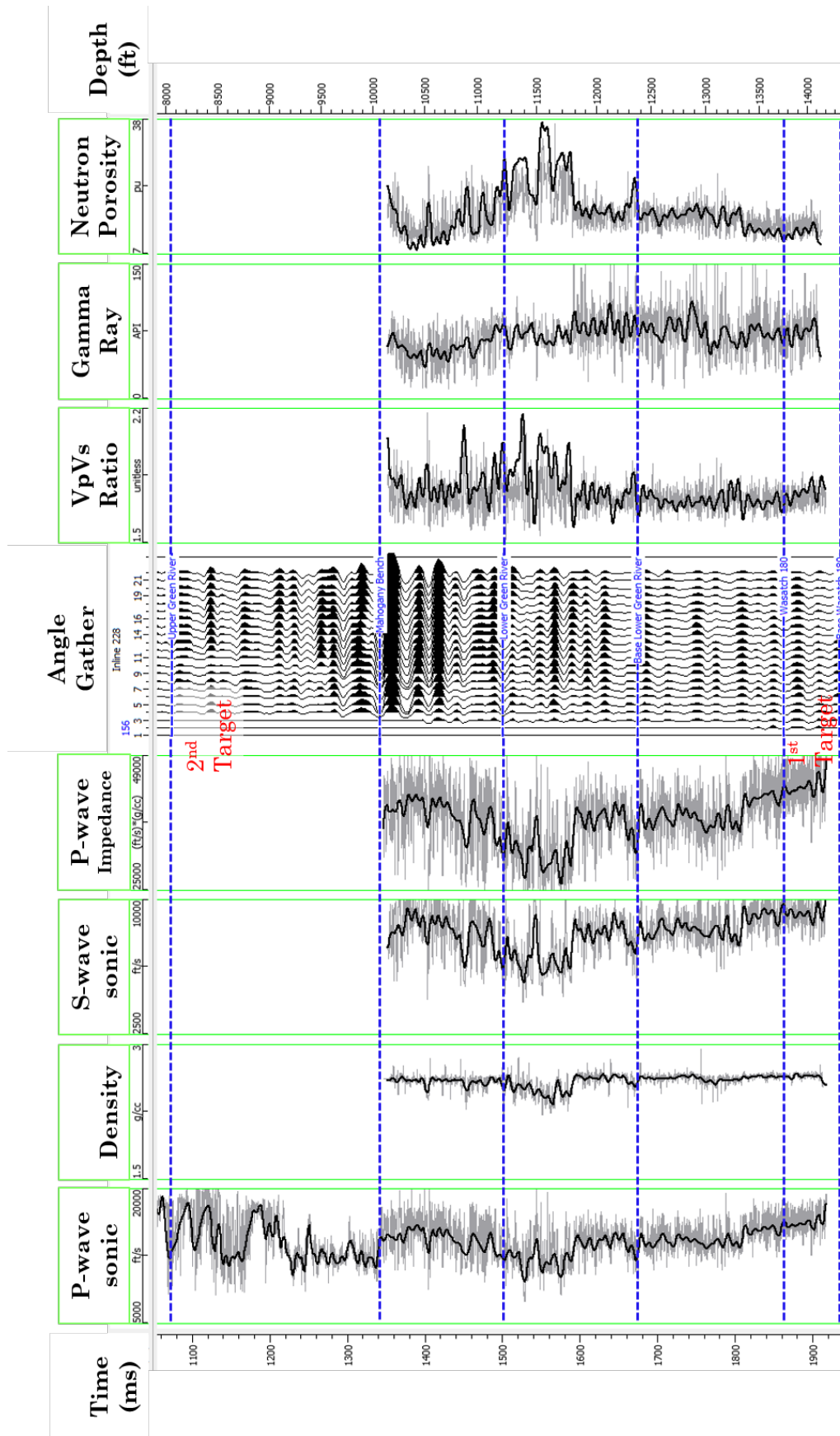


Figure 7 Available well log: grey indicates original logs, and black indicates filtered logs. Used filter is 100 Hz.

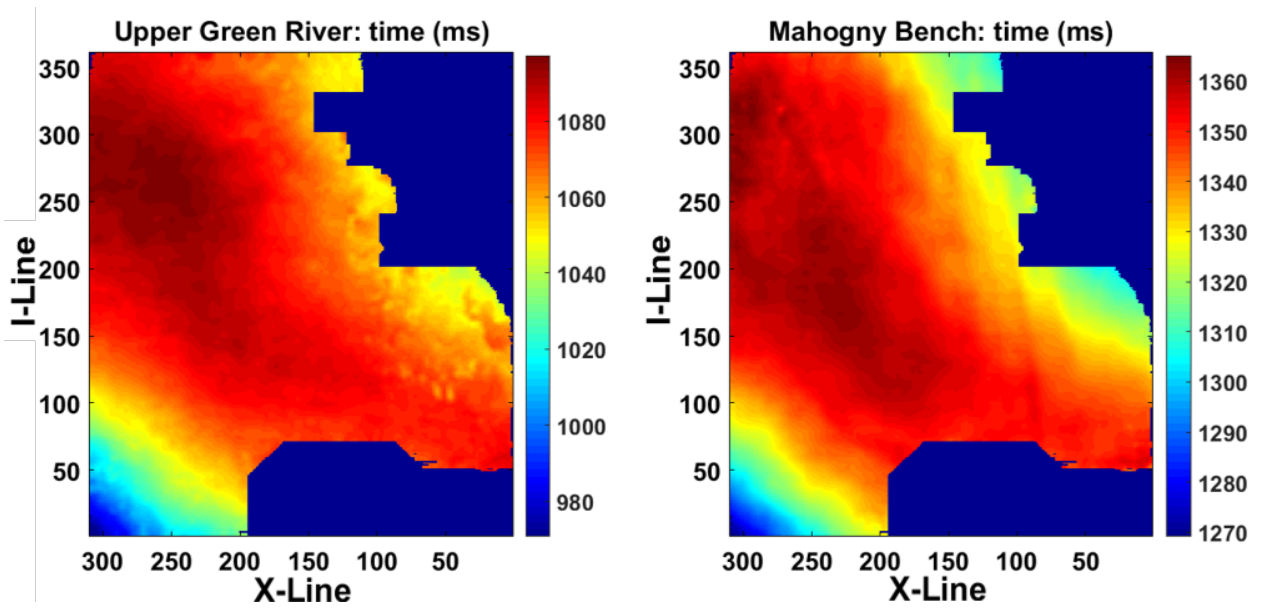


Figure 8 Two-way times in ms of Upper Green River formation.

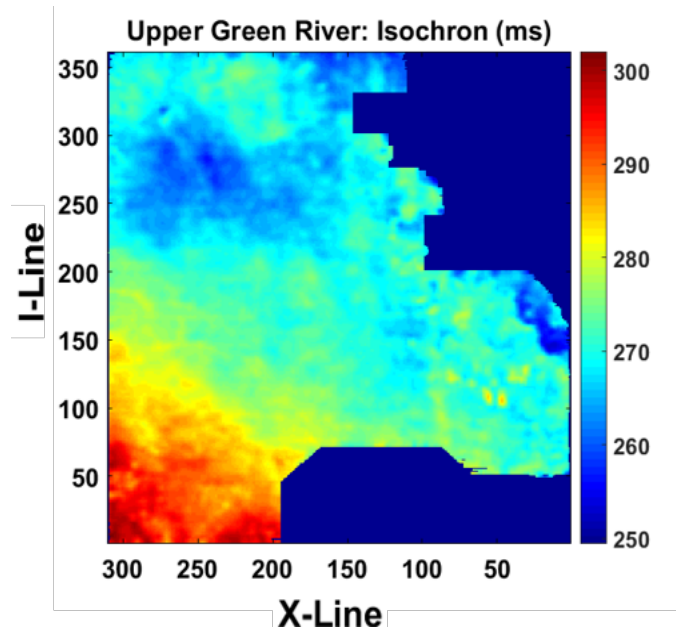


Figure 9 Isochrone of Upper Green River formation.

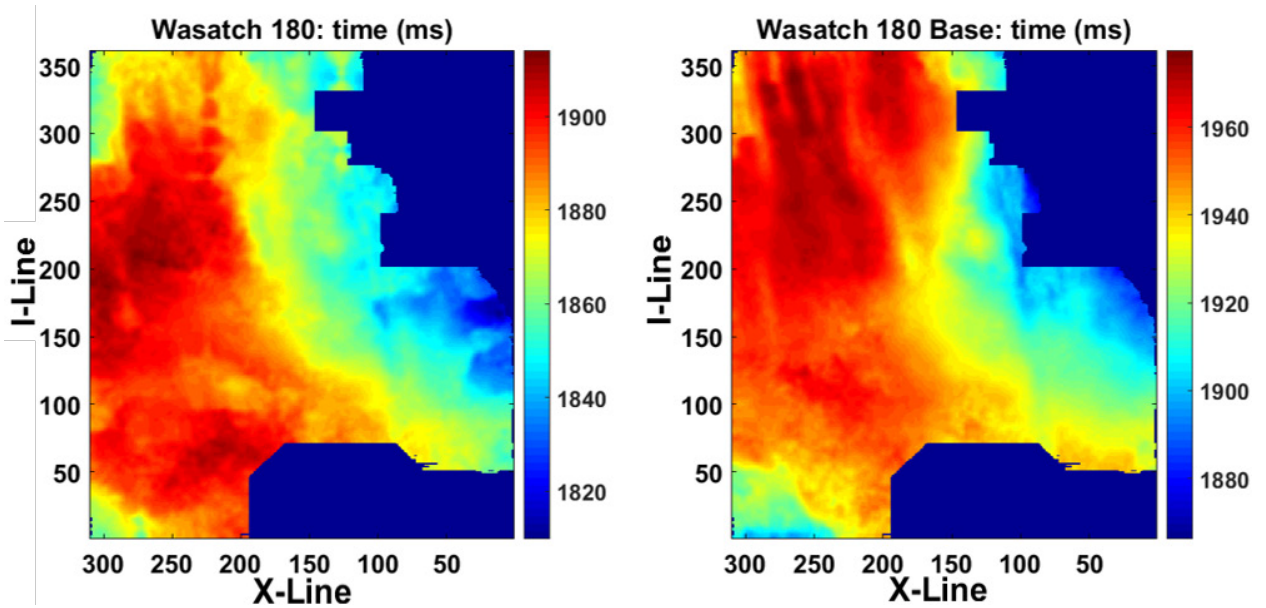


Figure 10 Two-way times in ms of Wasatch 180.

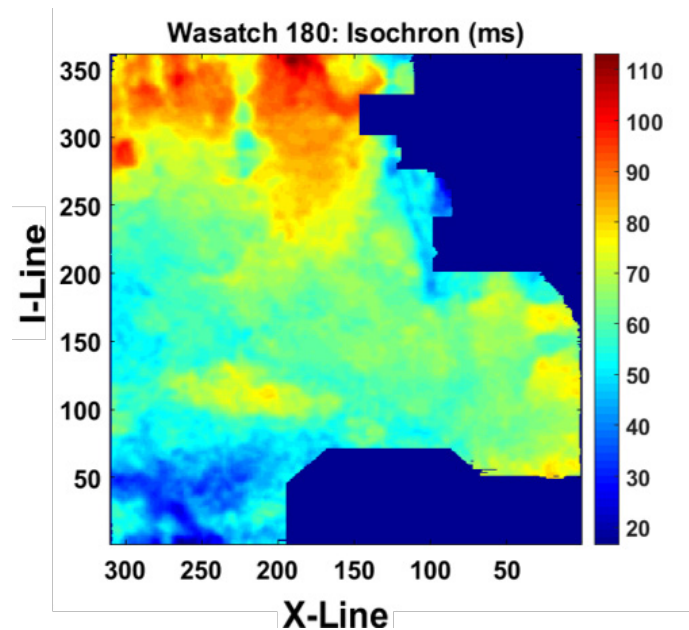


Figure 11 Isochrone of Wasatch 180. Unlike shallower target at Upper Green River formation, it thins out significantly towards the south part of the map.

AMPLITUDE VERSUS ANGLE (AVA) ANALYSIS

Zoeppritz (1919) derived equations that describe the conversion of an incident plane P wave at a velocity/density interface (Figure 12) with incident angle (θ) into four components: P-wave reflection (R_p), S-wave reflection (R_s), P-wave transmission (T_p),

and S-wave transmission (T_s). His derivation is valid for incident angles up to the critical angle under two assumptions. First, the displacement amplitudes are continuous at the interface between media that are in welded contacts (i.e., the media on both sides of the interface cannot be ripped apart). This condition can be called the kinematic boundary condition. Second, the stress tensor across the interface is continuous. This condition can be called the dynamic boundary condition. Note that these assumptions do not hold for vertical fractures because the displacement is not continuous at the interface for such media.

A popular approximation of the Zoeppritz equation for the P-wave reflection that is often used for AVA is given by Aki and Richards (1980). It relates reflection amplitude to incident angle and the three elastic parameters; P-wave velocity (α), S-wave velocity (β), and density (ρ). Shuey (1985) writes it as:

$$R_P(\theta) = A_{iso} + B_{iso} \sin^2(\theta) + C_{iso} \sin^2(\theta) \tan^2(\theta) \quad (7)$$

where

$$A_{iso} = \frac{1}{2} \left[\frac{\Delta\alpha}{\alpha} + \frac{\Delta\rho}{\rho} \right] \quad (8)$$

$$B_{iso} = \frac{1}{2} \frac{\Delta\alpha}{\alpha} - 4 \left[\frac{\bar{\beta}}{\alpha} \right]^2 \left[\frac{\Delta\beta}{\beta} + \frac{\Delta\rho}{2\rho} \right] \quad (9)$$

$$C_{iso} = \frac{1}{2} \frac{\Delta\alpha}{\alpha} \quad (10)$$

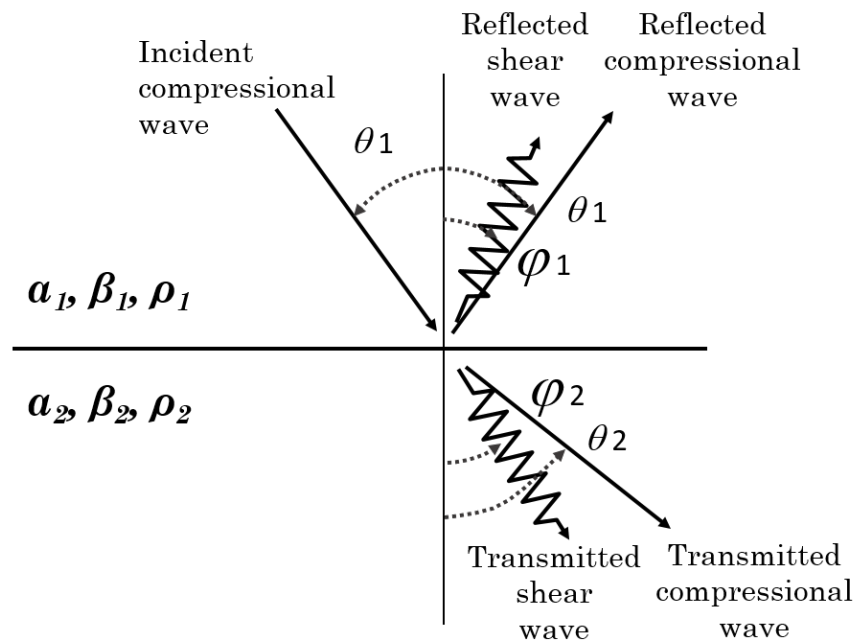


Figure 12 Incident P-wave energy partitioning into P-wave reflection and transmission and S-wave reflection and transmission at a welded contact interface.

The overbar in Equations (9) to (11) represents the average value at the interface between the upper and lower layers, while the capital delta represents the difference between the values for the upper and the lower layer. The advantage of this representation is that the reflection coefficient as a function of incident angle can be represented by a curve that has an intercept (A_{iso}) that is equivalent to normal-incidence reflection coefficient, a slope or first derivative of the curve (B_{iso}), and a gradient or second derivative of the curve (C_{iso}). This representation is called *ABC* method and very useful since it extract empirical information about the AVO. Such information can be plotted in cross plots as in the right of Figure 13. A positive impedance contrast means a positive normal-incidence reflection coefficient or a positive intercept. The slope is positive if the amplitude is increasing as incident angle increases and negative the amplitude is decreasing. The magnitude of the slope indicates the AVA strength. Shuey (1985) showed mathematically that Poisson’s ratio is the parameter most directly related to AVA strength for incident angles up to 30°. Slope and gradient are the basis for AVA classifications. Figure 13 shows different classes of AVA based on intercept and slope. The third term, curvature, becomes important for incident angles larger than 20°.

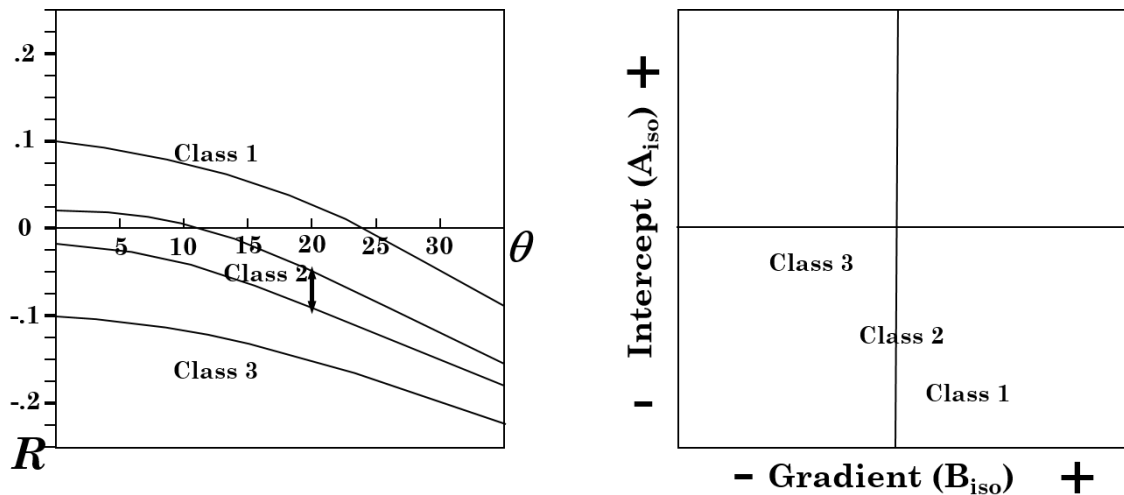


Figure 13 AVA 3 classes represented on reflectivity vs. incident angle plot (left) and on intercept vs. gradient plot (right).

Another useful representation of Aki and Richards (1980) is Fatti et al. (1994):

$$R_P(\theta) = c_1 R_P + c_2 R_S + c_3 R_\rho, \tag{11}$$

where

$$c_1 = 1 + \tan^2 \theta \quad (12)$$

$$c_2 = -8 \left[\frac{\bar{\beta}}{\bar{\alpha}} \right]^2 \sin^2(\theta) \quad (13)$$

$$c_3 = -\frac{1}{2} \tan^2(\theta) + 2 \left[\frac{\bar{\beta}}{\bar{\alpha}} \right]^2 \sin^2(\theta) \quad (14)$$

$$c_3 = -\frac{1}{2} \tan^2(\theta) + 2 \left[\frac{\bar{\beta}}{\bar{\alpha}} \right]^2 \sin^2(\theta) \quad (15)$$

$$R_P = \frac{1}{2} \left[\frac{\Delta\alpha}{\bar{\alpha}} + \frac{\Delta\rho}{2\bar{\rho}} \right] \quad (16)$$

$$R_S = \frac{1}{2} \left[\frac{\Delta\beta}{\bar{\beta}} + \frac{\Delta\rho}{2\bar{\rho}} \right], \quad (17)$$

and

$$R_\rho = \frac{\Delta\rho}{2\bar{\rho}} \quad (18)$$

This representation separates the reflection coefficient for P-wave data into three terms. The first and the second terms are related to normal incidence reflection coefficients, while the third term is related to density contrast. In fact, we have used this representation to invert for the three elastic parameters (α , β , and ρ). In order to do so, the small reflectivity approximation that relates P-wave reflectivity, R_P , to P-wave impedance, Z , is often used (Russell and Hampson, 2006):

$$R_P(i) = \frac{Z(i+1)-Z(i)}{Z(i+1)+Z(i)} \cong \frac{1}{2} [l_P(i+1) - l_P(i)], \quad (19)$$

where i denotes the interface between layers $i+1$ and i for a system of $n+1$ layers, and $l_P = \ln(Z_P)$. Equation (20) can be written into matrix form:

$$\begin{bmatrix} R_P(1) \\ R_P(2) \\ \vdots \\ R_P(n) \end{bmatrix} = \frac{1}{2} \begin{bmatrix} -1 & 1 & 0 & \dots \\ 0 & -1 & 1 & \dots \\ 0 & 0 & -1 & \dots \\ \vdots & \vdots & \vdots & \ddots \end{bmatrix} \begin{bmatrix} l_P(1) \\ l_P(2) \\ \vdots \\ l_P(n) \end{bmatrix}, \quad (20)$$

where the second matrix represents the derivative matrix, D . Then, the seismic trace, $s(s_1, s_2, \dots, s_n)$, can be expressed as matrix convolution of the wavelet $w(w_1, w_2, \dots, w_k)$ with reflectivity:

$$\begin{bmatrix} s_1 \\ s_2 \\ \vdots \\ s_n \end{bmatrix} = \frac{1}{2} \begin{bmatrix} w_1 & 0 & 0 & \cdots \\ w_2 & w_1 & 0 & \cdots \\ 0 & w_2 & w_1 & \cdots \\ \vdots & \vdots & w_2 & \ddots \end{bmatrix} \begin{bmatrix} -1 & 1 & 0 & \cdots \\ 0 & -1 & 1 & \cdots \\ 0 & 0 & -1 & \cdots \\ \vdots & \vdots & \vdots & \ddots \end{bmatrix} \begin{bmatrix} l_p(1) \\ l_p(2) \\ \vdots \\ l_p(n) \end{bmatrix} \quad (21)$$

Equation (22) can be used for post-stack P-wave impedance inversion using conjugate gradient method with a starting initial guess model. However, it needs to be extended for angle gathers to be used for pre-stack elastic inversion. For an angle gather, $s(\theta)$, Equation (22) and Equation (12) can be combined:

$$s(\theta) = \frac{1}{2} c_1 w(\theta) D l_p + \frac{1}{2} c_2 w(\theta) D l_s + \frac{1}{2} c_3 w(\theta) D l_\rho \quad (22)$$

A relation between l_p and l_s and between l_p and l_ρ are derived from Gardner's rule assuming that $\frac{\beta}{\alpha}$ is constant for a wet trend. The relationships are:

$$l_s = k l_p + k_c + \Delta l_s \quad (23)$$

and

$$l_\rho = m l_p + m_c + \Delta l_\rho \quad (24)$$

where k , k_c , m , and m_c are constants.

The wavelet, w , is extended to varying wavelet for different angle of incidence, $w(\theta)$. Equations (23), (24), and (25) are combined into

$$T(\theta) = \tilde{c}_1 w(\theta) D l_p + \tilde{c}_2 w(\theta) D \Delta l_s + w(\theta) c_3 D \Delta l_\rho \quad (25)$$

where

$$\tilde{c}_1 = \frac{1}{2} c_1 + \frac{1}{2} k c_2 + m c_3 \quad (26)$$

and

$$\tilde{c}_2 = \frac{1}{2} c_2 \quad (27)$$

Equation (23) can be rewritten into matrix form:

$$\begin{bmatrix} s(\theta_1) \\ s(\theta_2) \\ \vdots \\ s(\theta_n) \end{bmatrix} = \begin{bmatrix} \tilde{c}_1(\theta_1)w(\theta_1)D & \tilde{c}_2(\theta_1)w(\theta_1)D & \tilde{c}_3(\theta_1)w(\theta_1)D \\ \tilde{c}_1(\theta_2)w(\theta_2)D & \tilde{c}_2(\theta_2)w(\theta_2)D & \tilde{c}_3(\theta_2)w(\theta_2)D \\ \vdots & \vdots & \vdots \\ \tilde{c}_1(\theta_n)w(\theta_n)D & \tilde{c}_2(\theta_n)w(\theta_n)D & \tilde{c}_3(\theta_n)w(\theta_n)D \end{bmatrix} \begin{bmatrix} l_p \\ \Delta l_s \\ \Delta l_\rho \end{bmatrix} \quad (28)$$

Similar to Equation (25), Equation (29) is solved using a conjugate gradient method with an initial guess model. Figure 14 shows a crossplot of l_p vs l_ρ and l_p vs l_s . The deviation between the best fit line and outliers, Δl_ρ and Δl_s , may be the hydrocarbon

anomalies. The elastic parameters are first inverted and QCed at the well locations. A synthetic gather is calculated using convolutional model. The model can be calculated using a convolutional model based on the Zoeppritz (1919) equations or on the linearized equations, i.e., Aki and Richards (1980).

The angles used for the inversion were limited to those less than or equal to 30° because the correlation between linearized Zoeppritz calculated data and measured data becomes poor when using larger angles, as shown by Figure 14 and Figure 15. Comparing the two figures, the slope when using larger angles seem to be flipped. Therefore, we used only small angles up to 30°, which also make us avoid critical angles that violates the assumptions made for linearized AVO. A comparison of Figure 16 to Figure 13, indicates that the Upper Green River is likely AVA class 3.

The inversion results, the initial model, and original logs for one of the available wells are shown by Figure 17. Initial model is indicated by black, while original logs are indicated by blue. Also, the angle gather in red is compared to the synthetic gather in blue. The three elastic parameters, V_p , V_s , and ρ for isotropic medium are inverted for at the locations of the six available wells. The AVA inversion was carried for the pre-stack volume.

Two data slices were created across each reservoir from the inversion results. The first slice is for P-wave impedance and shown by Figure 18 for Upper Green River formation (left) and for Wasatch 180 (right). The second slice is for V_p/V_s ratio and shown by Figure 19 for Upper Green River formation (left) and for Wasatch-180 (right).

These data slices show the six available wells used for parameter correlation and for the initial model. Accumulative production data for oil and gas were provided for different set of wells. Wells were drilled over a period of more than 40 years. Therefore, comparison of older well to newer ones would not be reasonable. In the Upper Green River, some correlation seems to exist between abnormally productive gas wells and low P-wave impedances. However, in general, abnormally productive oil wells do not correlate to either P-wave impedance or V_p/V_s ratio maps. Morgan et al. (2003) have concluded that neither structure nor stratigraphy help predict the largest oil production areas within the field.

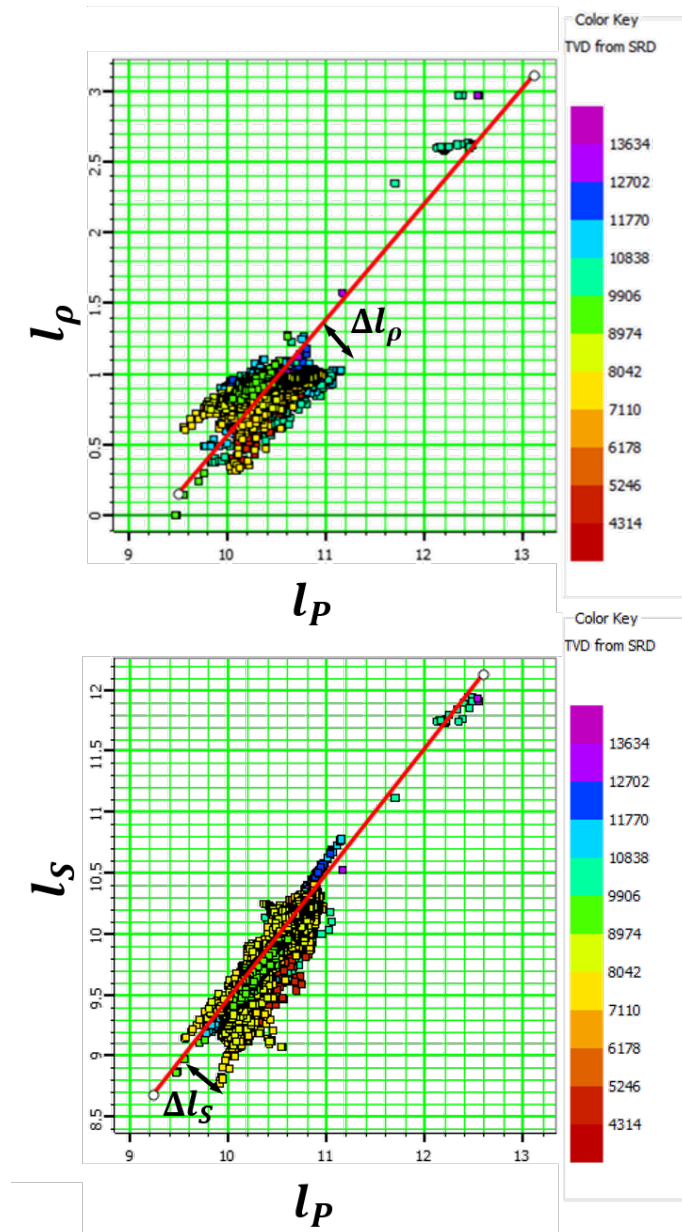


Figure 14 Crossplots of l_p vs l_p (upper) and l_p vs l_s (lower). The deviation between the best fit line and outliers, Δl_p and Δl_s , may be the hydrocarbon anomalies.

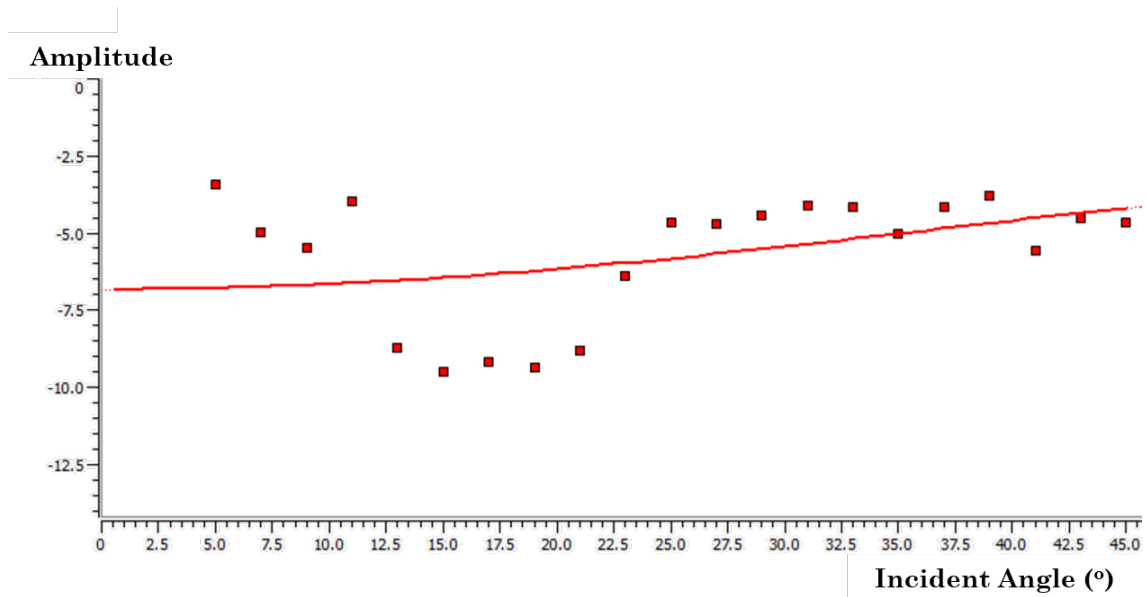


Figure 15 AVA: amplitude vs incident angle plot for one gather at Upper Green River. Incident angles ranges up to 45°. Correlation between theoretical and measured data is poor. Also, notice that the sign of the slope is flipped, and AVO class is not 3 anymore.

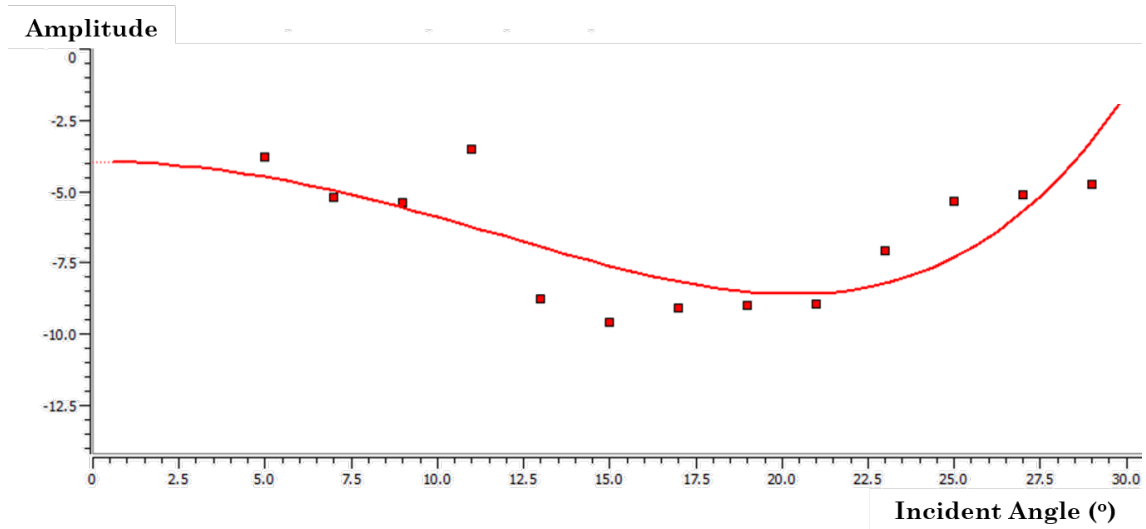


Figure 16 AVA: amplitude vs incident angle plot for one gather at Upper Green River. AVA class is 3. Incident angles ranges up to 30°. Correlation between theoretical and measured data is good.

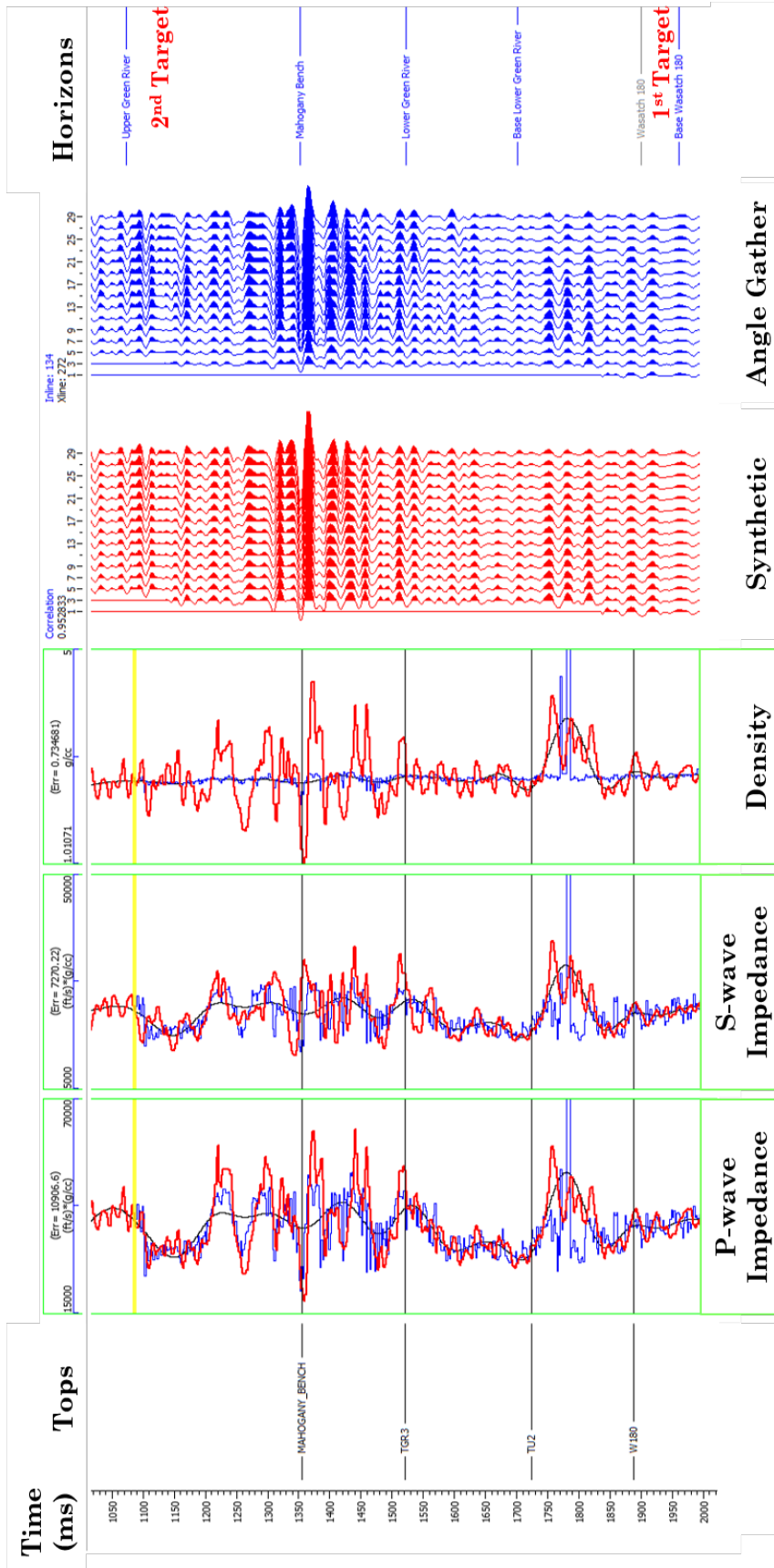


Figure 17 AVA inversion results indicated by red. Initial model is indicated by black, while original logs are indicated by blue.

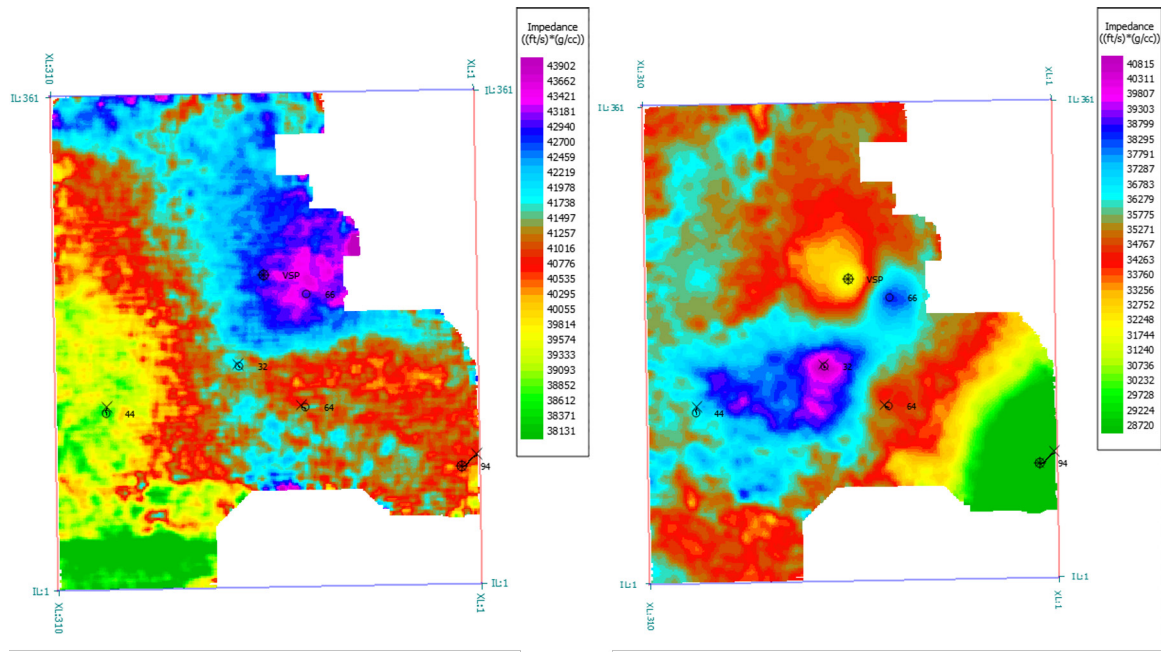


Figure 18 AVA inversion: horizon slice of inverted P-wave impedance of Upper Green River formation (left) and Wasatch 180 (right).

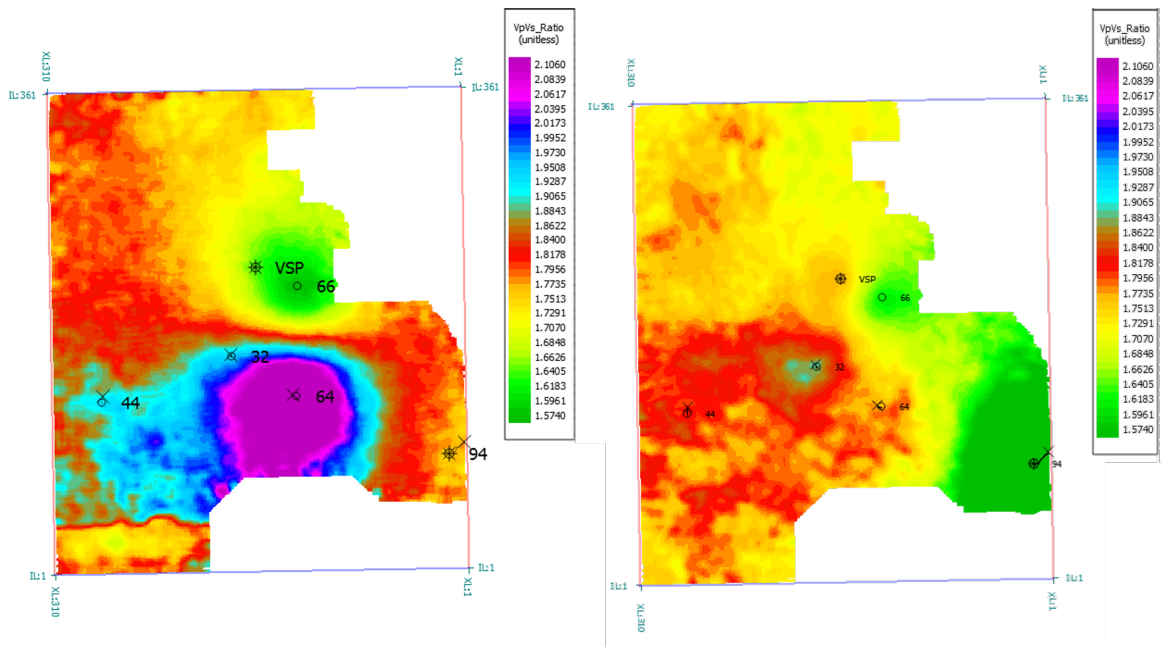


Figure 19 AVA inversion: horizon slice of inverted Vp/ Vs of Upper Green River formation (left) and Wasatch 180 (right).

AMPLITUDE VERSUS AZIMUTH (AVAZ) ANALYSIS

Ruger (1998) derived the reflection and transition function for different scenarios of transversely isotropic medium. His approximations include the PP, PS and SS waves for VTI and HTI cases. His approximation is valid for pre-critical incidence angles on an interface between two weakly anisotropic HTI media with the same direction of axis of symmetry and small jumps in the elastic properties across the boundary (Ruger, 1998). Vavryčuk and Pšenčík, (1998) derived the reflection and transmission coefficients for interface separating two weak but arbitrary anisotropic media.

The stiffness tensors for HTI and VTI medium are different because of different directions of symmetry axes as defined by (Musgrave, 1970; Ruger,1996)

$$c^{HTI} = \begin{bmatrix} c_{11} & c_{13} & c_{13} & 0 & 0 & 0 \\ c_{13} & c_{33} & (c_{33} - 2c_{44}) & 0 & 0 & 0 \\ c_{13} & (c_{33} - 2c_{44}) & c_{33} & 0 & 0 & 0 \\ 0 & 0 & 0 & c_{44} & 0 & 0 \\ 0 & 0 & 0 & 0 & c_{55} & 0 \\ 0 & 0 & 0 & 0 & 0 & c_{55} \end{bmatrix} \quad (290)$$

and

$$c^{VTI} = \begin{bmatrix} c_{11} & (c_{11} - 2c_{66}) & c_{13} & 0 & 0 & 0 \\ (c_{11} - 2c_{66}) & c_{11} & c_{13} & 0 & 0 & 0 \\ c_{13} & c_{13} & c_{33} & 0 & 0 & 0 \\ 0 & 0 & 0 & c_{44} & 0 & 0 \\ 0 & 0 & 0 & 0 & c_{44} & 0 \\ 0 & 0 & 0 & 0 & 0 & c_{66} \end{bmatrix} \quad (30)$$

HTI and VTI media have five independent parameters. For VTI media, Thomsen (1986) defined three anisotropic parameters (δ , ϵ , and ϵ) together with two velocity parameters (α and β), where $\alpha = V_{P0}$ (the vertical P-wave velocity) and $\beta = V_{S0}$ (the vertical S-wave velocity). Those five parameters completely define VTI, and can be written in terms of the density ρ and the stiffness coefficients:

$$\alpha = \sqrt{\frac{c_{33}}{\rho}} \quad (31)$$

$$\beta = \sqrt{\frac{c_{44}}{\rho}} \quad (32)$$

$$\delta = \frac{(c_{13}+c_{44})^2-(c_{33}+c_{44})^2}{2c_{33}(c_{33}-c_{44})} \quad (33)$$

$$\epsilon = \frac{c_{11}-c_{33}}{2c_{33}} \quad (34)$$

$$\gamma = \frac{c_{66}-c_{44}}{2c_{44}} \quad (35)$$

The constant ϵ can be thought of as the fractional difference of the P-wave velocities in the horizontal direction and the vertical direction, while the constant γ measures the fractional difference of the S-wave velocity in the horizontal direction and the vertical direction. The reflectivity, in an HTI medium, depends on both incident angle and azimuth and is given by:

$$R_P(\theta, \phi) = \frac{1}{2} \frac{\Delta z}{z} + \frac{1}{2} \left(\left[\frac{\Delta \alpha}{\bar{\alpha}} - 4 \left[\frac{\bar{\beta}}{\bar{\alpha}} \right]^2 \frac{\Delta G}{G} \right] + \left[\Delta \delta^{(v)} + 8 \left[\frac{\bar{\beta}}{\bar{\alpha}} \right]^2 \Delta \gamma \right] \cos^2(\phi) \right) \sin^2(\theta) + \frac{1}{2} \left(\frac{\Delta \alpha}{\bar{\alpha}} + \Delta \epsilon^{(v)} \right) \cos^4(\phi) + \Delta \delta^{(v)} \sin^2(\phi) \cos^2(\phi) \sin^2(\theta) \tan^2(\theta) \quad (37)$$

Because of the presence of vertical fractures, $\beta (= V_{S0})$ is defined in the HTI case as the velocity of the vertical S wave polarized parallel to the isotropy plane. $G = \rho \beta^S$ is S-wave modulus. The operator Δ is the differential operator on the bedding boundaries. The angle between the symmetry axis measured from North, ϕ_s , and the source-receiver azimuth measured from North, ϕ_g , is given by $\phi = \phi_g - \phi_s$. The S-wave velocity (β) and the anisotropic parameters are defined in terms of stiffness coefficients with the following relationships:

$$\beta = \sqrt{\frac{c_{55}}{\rho}} \quad (38)$$

$$\delta^{(v)} = \frac{(c_{13}+c_{55})^2-(c_{33}+c_{55})^2}{2c_{33}(c_{33}-c_{55})} \quad (39)$$

$$\epsilon^{(v)} = \frac{c_{11}-c_{33}}{2c_{33}} \quad (40)$$

$$\gamma = \frac{c_{44}-c_{66}}{2c_{66}} \quad (41)$$

$\epsilon^{(v)}$ is negative to zero in the case of HTI because that horizontal P-wave velocity traveling perpendicular to fractures cannot be higher than P-wave velocity. It can be negligibly small or zero (Thomsen, 1995) or small and negative (Tsvankin, 1997). Although HTI is useful to describe vertically fractured rocks, it is only true for penny-shaped cracks (Delbecq et al., 2013). Bakulin et al. (2000a) Bakulin et al. (2000b) described methods that are useful for lower symmetry than HTI. For AVAZ inversion, HTI assumption may be sufficient because the deviation from HTI is small relative to signal-to-noise ratio and a form of Equation (37) that is similar to the Shuey (1985) form of AVA of Equation (8) was used after ignoring the third term that relates to large incident angles:

$$R_p(\theta, \phi) = A_{iso} + (B_{iso} + B_{ani} \cos^2(\phi)) \sin^2(\theta) \quad (36)$$

where

$$B_{ani} = \frac{1}{2} \Delta \delta^{(v)} + 8 \left(\frac{\bar{\beta}}{\bar{\alpha}} \right)^2 \Delta \gamma \quad (37)$$

The azimuthal angle (ϕ) is the difference between the source-receiver azimuth and one of the model parameters that is to be inverted for ϕ_s . The other model parameters are A_{iso} , B_{iso} , and B_{ani} . The objective function is the sum of the square of the differences between the measured data and theoretical data, $R_p(\theta, \phi)$, modeled using Ruger (1998). For the AVAZ done in this thesis, I used an iterative nonlinear optimization called the Barrier method (similar to Newton's method) to minimize the objective function. The optimization code calculates and employs full Jacobian and sparse Hessian matrices to search for the minimum of the objective function. The anisotropic gradient, B_{ani} , as function of azimuth forms an ellipse. Therefore, higher azimuthal coverage translates into more accurate fitting of ellipse. Due to the nonlinearity of Equation (42), the solution is not unique and yields two possible orientations of symmetry axis, ϕ_s , orthogonal to each other (Ruger, 1996).

To test the algorithm, a synthetic gather was created using the velocities and densities from well logs and assumed values for $\delta^{(v)}$ and γ . The synthetic gather is displayed on Figure 20. After 24 iterations of the optimization routine, the isotropy plane was obtained to be 35° ; the intercept, isotropic gradient, and anisotropic gradient were estimated to be -0.057, 1.36, and 0.07, respectively (the intercept can be seen on Figure 21). The values for anisotropic gradient and isotropy plane obtained by inversion were identical to the values used for forward modeling of the synthetic data.

A single pre-stack reflection was picked on COV gathers for the measured data. $R_p(\theta, \phi)$ is the theoretical data using Ruger (1998). For the stability of the inversion, only full fold (larger than 160) COV gathers was used. The full fold base map is shown in Figure 22. Also, the pre-stack amplitude values were borrowed from eight neighboring gathers for each gather. Therefore, pre-stack measured data were used nine times; once in its location and eight times by neighboring locations. The angles of incidence (θ) are calculated using Snell's Law as described above. The incidence angles that were used are up to 45° because of the dense azimuthal coverage from 30 to 40° angles of incidence. Figure 23 shows the azimuthal coverage of a single COV gather for different angles of incidence.

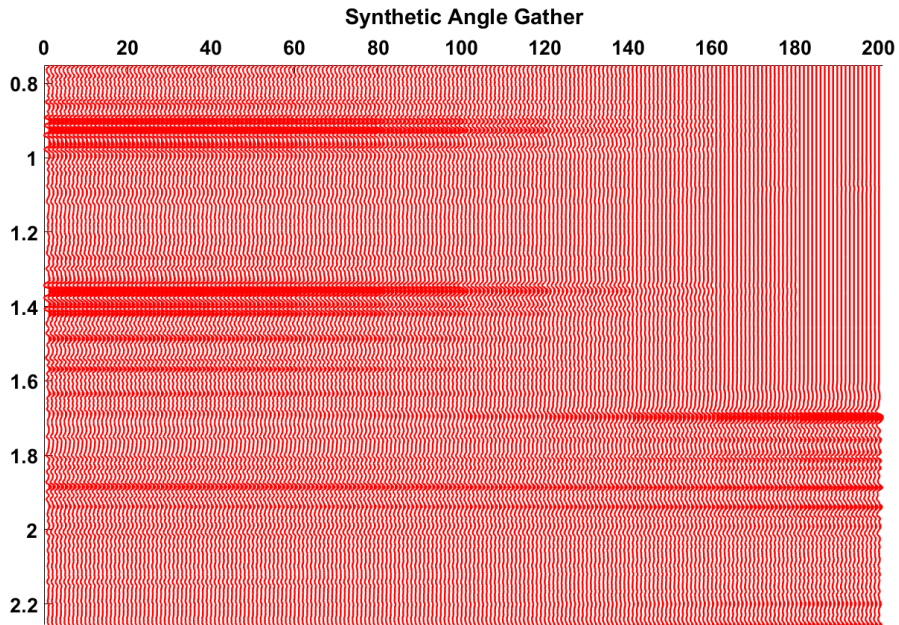


Figure 20: Synthetic angle gathers.

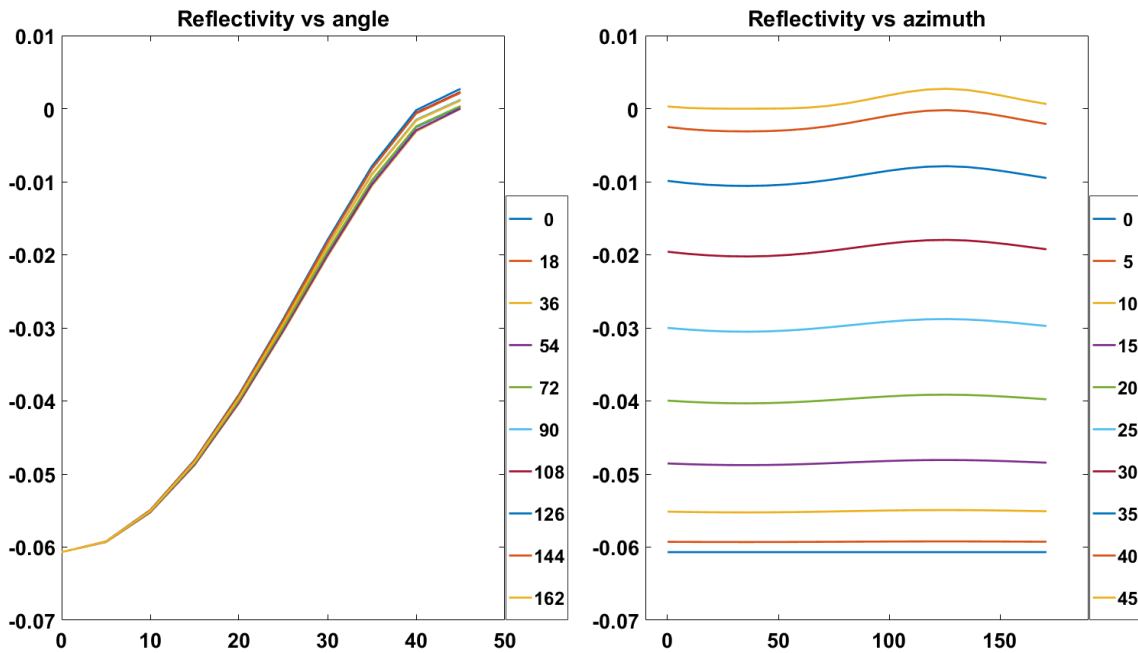


Figure 21 Amplitude vs incident angles for different azimuths indicated by curves of different colors (left) and Amplitude vs azimuth for different incident angles azimuths indicated by curves of different colors (right).

The amplitude of a single COV gathers as function of offset for different azimuths can be seen by Figure 25. The initial model was set to $(\phi_s, A_{iso}, B_{iso}, B_{ani} = 0.1, 0.1, 0.1, 0.1)$. The model parameters were updated through many iterations of the Barrier optimization algorithm until the objective function was minimized to be less than a small fraction. On average, 25 iterations were required at each CDP location. The final Normalized-Root-Mean-Square (NRMS) error between the pre-stack theoretical and measured values at each CDP location is shown on Figure 26 for Upper Green River formation (left) and Wasatch 180 (right).

For penny-shaped cracks model (Hudson, 1981), B_{ani} can be proportional to the crack density, as shown by Figure 26. For simplicity, this rock physics model is often used by industry; I do so here. The ambiguity in inverted symmetry axis can be resolved by some priori information, such a rough estimate of B_{ani} or knowledge about symmetry axis directions (Ruger, 1996). For an external constrain, a correlation between AVAZ and VVAZ symmetry orientation can be calculated per horizon for positive and then negative B_{ani} . The better correlation decides the sign of B_{ani} and 90° is added to ϕ_s in the case of B_{ani} sign being altered. For the shallower gas reservoir (Upper Green River), the sign of B_{ani} was constrained to positive. According to Equation (43), the positive sign seems physical because it is the first fractured reservoir and the second term is positive and larger than the absolute value of the first negative term. The deeper oil reservoir (Wasatch 180) is overlain by several fractured reservoirs and it is hard to estimate a sign for B_{ani} physically, but a sign was estimated after correlation with VVAZ.

A second shortcoming of AVAZ inversion is that, unlike VVAZ inversion, the anisotropy of overburden and shallower layers cannot be stripped out for the reservoirs. Its main advantage is that, like other amplitude-based methods, it has a high resolution as discussed by Al Dulaijan (2017).

AVAZ inversion results for the Upper Green River formation and Wasatch 180 horizons are shown in Figure 27 and Figure 28 respectively. On the left of those two figures is the B_{ani} that indicates the intensity of azimuthal anisotropy, and on the right is the orientation of the symmetry plane. The Upper Green River formation has two main directions of symmetry plane. The major trend is indicated by green and it is oriented NW-SE at -20° from North (or 20° from North counterclockwise). The minor trend is 40° from North clockwise. The major trend correlates well to high positive and high negative values of B_{ani} . On the other hand, Wasatch 180 reservoir has symmetry plane oriented NE-SW at 5° from North clockwise. The B_{ani} values of Wasatch 180 are greater than those of Upper Green River formation. According to the penny-shaped fracture model (Hudson, 1980), this means that the Wasatch 180 is more intensely fractured than the Upper Green River.

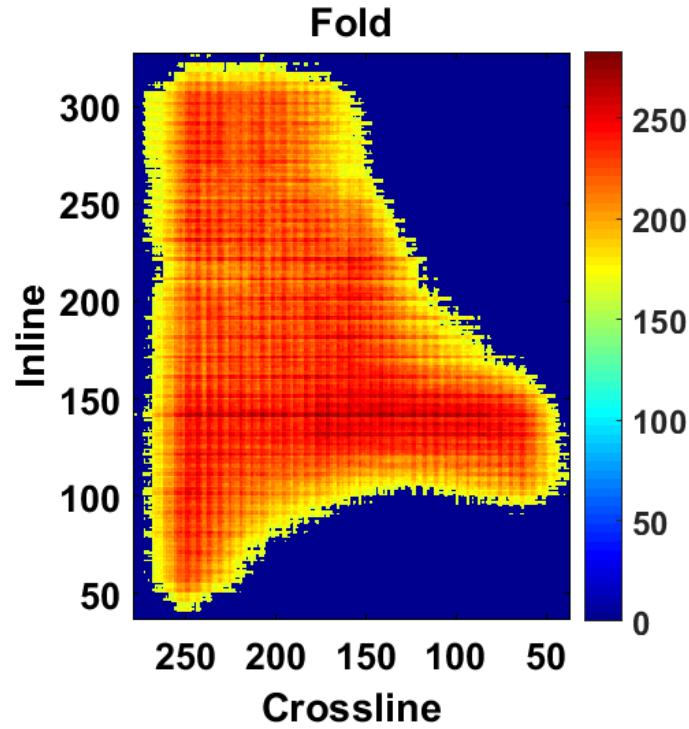


Figure 22 Base map of full fold (larger than 160) seismic used for AVAZ inversion.

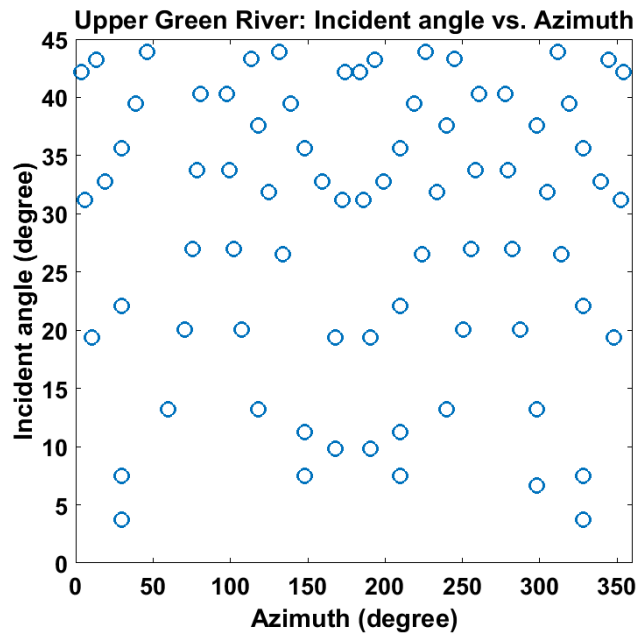


Figure 23 Azimuth vs incident angle distribution of a single gather at the Upper Green River horizon. Notice the dense coverage from 30° to 40° angles of incidence.

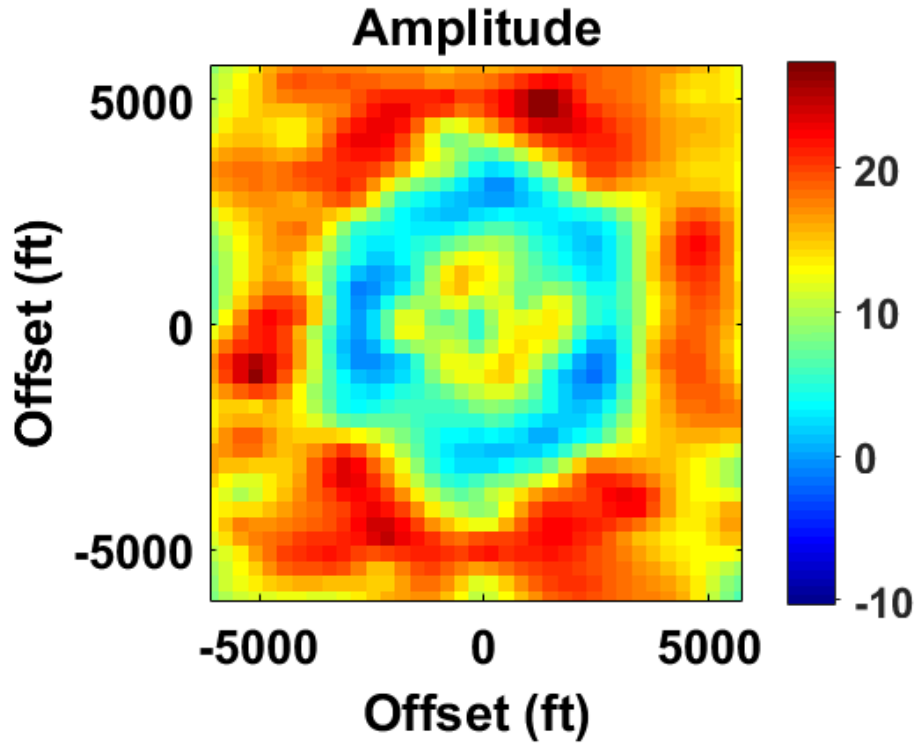


Figure 24 Amplitudes of a single prestack gather for different azimuths and offsets.

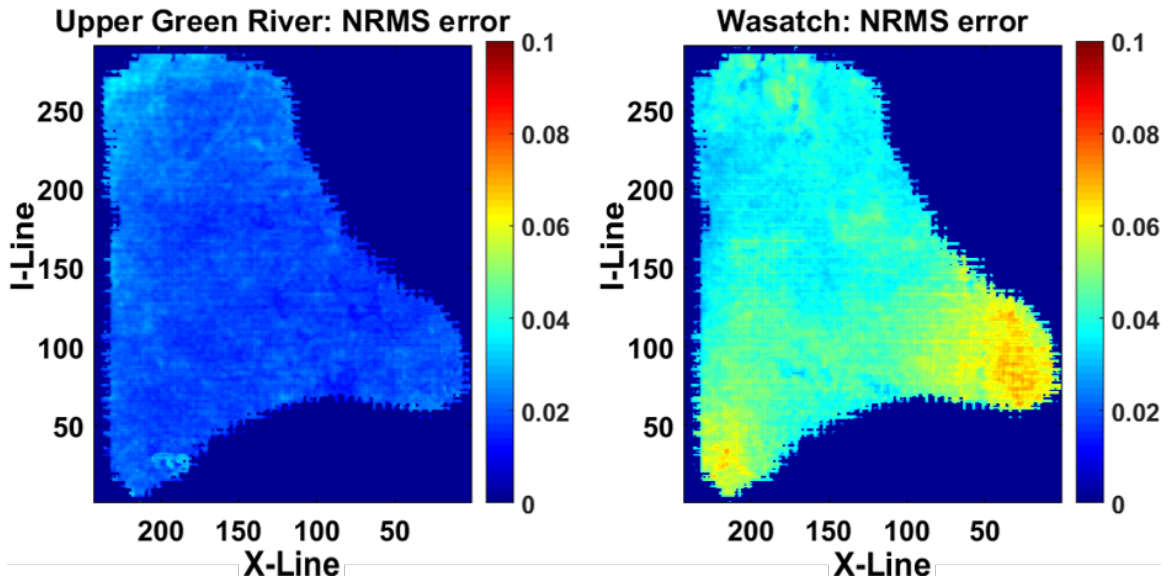


Figure 25 NRMS error between theoretical and measured data for Upper Green River formation (left) and Wasatch 180 (right)

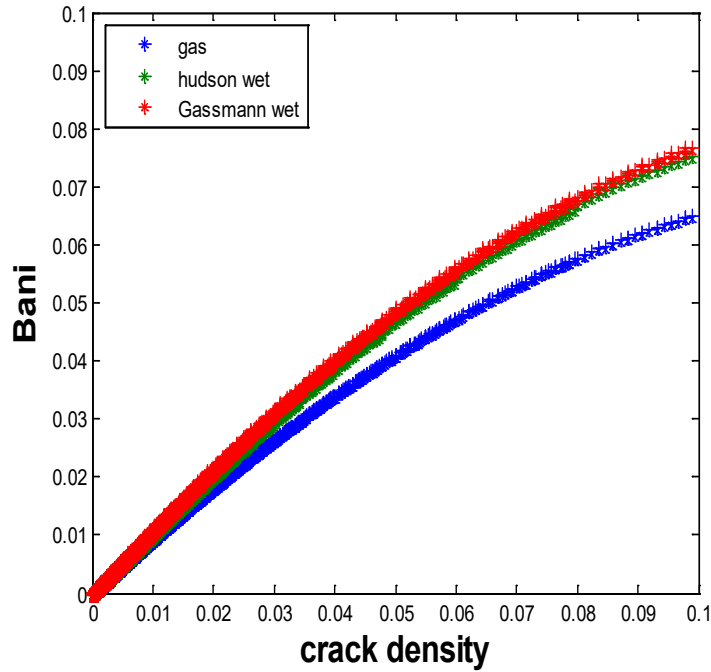


Figure 26 B_{ani} vs. crack density of penny-shaped fractures for gas (blue), Hudson wet (Green), and Gassmann wet (red). (after Downton, 2016)

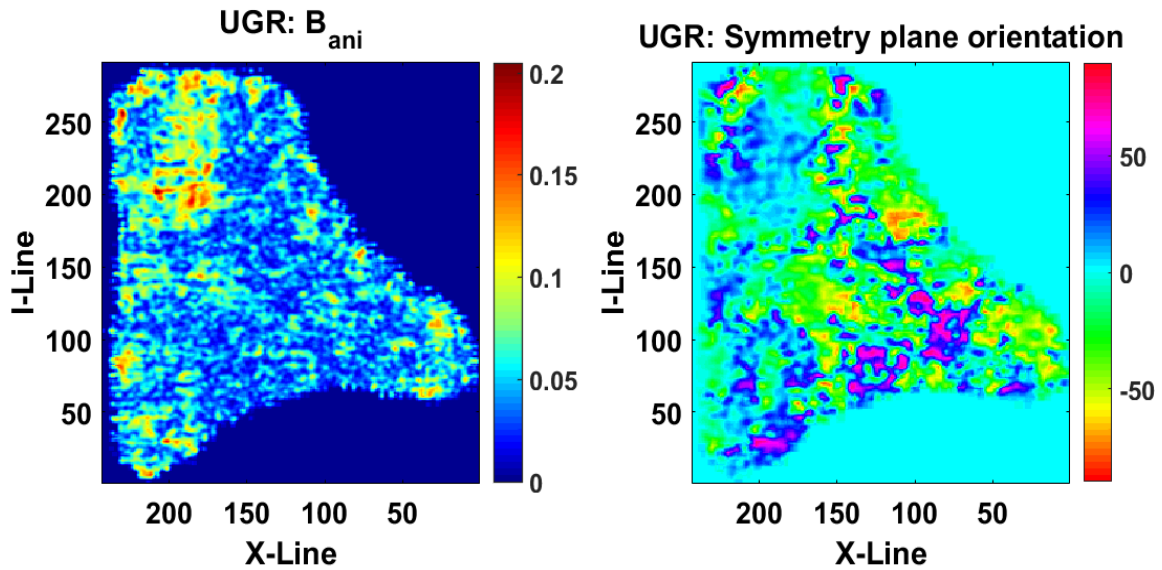


Figure 27 AVAZ inversion for Upper Green River: Bani horizon (left), symmetry plane orientation horizon (middle), and symmetry plane orientation circular histogram (right).

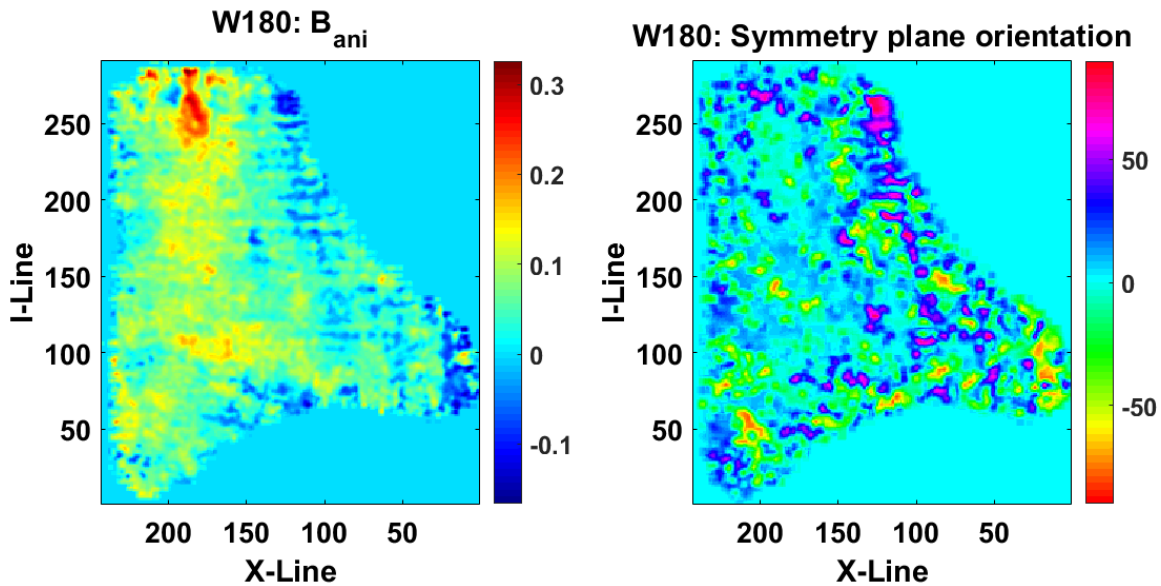


Figure 28 AVAZ inversion for Wasatch 180: Bani horizon (left), symmetry plane orientation horizon (right).

ACKNOWLEDGEMENTS

We thank the sponsors of CREWES for their support. We also gratefully acknowledge support from NSERC (Natural Science and Engineering Research Council of Canada) through the grant CRDPJ 379744-08. Also, we are grateful to Devon Energy for permission to use the seismic data and publish the results and to LINN Energy for permission to use wells data and publish the results. We thank CGGVeritas for the use of Geoview® by Hampson-Russell software. The first author would like to thank Dr. Jon Downton, Dr. Hassan Khaniani, Mohammed Kanfar, and Khalid Almuteri for useful discussions. He thanks Dr. Joe Wong for proofreading this report. Also, he would like to thank Saudi Aramco for graduate study sponsorship.

SUMMARY AND CONCLUSIONS

In this paper, AVA inversion (based on a simplified Zoeppritz equation) was used to estimate elastic stiffness coefficients from 3D prestack data acquired at the Altamont-Bluebell field. These estimated isotropic elastic stiffness coefficients can be useful for identifying sweet spots, i.e., zones of high hydrocarbon potential.

In addition, AVAZ inversion (based on a simplified Ruger's equation describing reflections from HTI media) was used to estimate four anisotropic parameters from azimuthally varying reflection amplitudes and NMO velocities. These estimated anisotropic parameters can be useful for estimating fracture density and orientation in subsurface rock formations. An ambiguity exists in the estimated fracture plane orientation. This ambiguity can be resolved by using results of VVAZ inversion as a priori information for the AVAZ inversion.

Because, the reservoirs of Altamont-Bluebell are unconventional and fractures play a significant role in production, anisotropy intensity and orientation maps were calculated

per reservoir top. The anisotropy plane orientation is found to have a major NW-SE trend for both reservoirs, while the anisotropy intensity is found to be greater for Wasatch-180 formation than Upper Green River formation. However, the interpretation of AVAZ inversion results in isolation is not recommended. Interpretation of the AVAZ results should be done in collaboration with the VVAZ inversion results.

REFERENCES

- Aki, K. and Richards, P.G., 1980, *Quantitative Seismology: Theory and Methods*, W.H.Freeman and Co., San Francisco, 932 pp.
- Al Dulaijan, K., 2008, Near-surface characterization using seismic refraction and surface-wave methods. Masters thesis: University of Calgary.
- Al Dulaijan, K., 2017, Inversion of azimuthal velocity and amplitude variations for seismic anisotropy. Ph.D. thesis: University of Calgary.
- Bakulin, A., Grechka, V., & Tsvankin, I., 2000b, Estimation of fracture parameters from reflection seismic data—Part II: Fractured models with orthorhombic symmetry. *Geophysics*, 65(6), 1803-1817.
- Bakulin, A., V. Grechka, and I. Tsvankin, 2000, Estimation of fracture parameters from reflection seismic data—Part I: HTI model due to a single fracture set, *Geophysics*, 65, 1788.
- Cary, P. W., 1999, Prestack imaging with 3-D common-offset-vector gathers. 11th Annual CREWES Report, 615-626.
- CGGVeritas, 2014, *GeoView: Hampson-Rusell software manual: Release 9.0*. Calgary.
- Delbecq, F., Downton, J. E., & Letizia, M., 2013, A math-free look at azimuthal surface seismic techniques. *CSEG Recorder*, 38(1), 20e31.
- Downton, J., 2016, *GeoView (ProAz): Hampson-Rusell software manual & course note: Release 10.1*. Calgary: CGGVeritas.
- Fatti, J. L., Smith, G. C., Vail, P. J., Strauss, P. J., & Levitt, P. R., 1994, Detection of gas in sandstone reservoirs using AVO analysis: A 3-D seismic case history using the Geostack technique. *Geophysics*, 59(9), 1362-1376.
- Hudson, J. A., 1988, Seismic wave propagation through material containing partially saturated cracks: *Geophysical Journal International*, 92, 33–37.
- Lay, D. C., 1996, *Linear algebra and its applications*, 2nd ed, Addison-Wesley.
- Li, X., 2008, An introduction to common offset vector trace gathering; *CSEG Recorder*, 33, no. 9, 28-34.
- Morgan, Craig D., J. Wallace Gwynn, M. Lee Allison, Richard Curtice, Milind D. Deo, Richard Jarrard, Thomas H. Morris, and Carol N. Tripp., 2003, Characterization of the Bluebell Oil Field, Uinta Basin, Duchesne and Uintah Counties, Utah (SS-106 Pt. 1).
- Musgrave, M. J. P., 1970. *Crystal acoustics: Introduction to the study of elastic waves and vibrations in crystals*. San Francisco: Holden-Day.
- Rüger, A. 1996. Reflection coefficients and azimuthal AVO analysis in anisotropic media. Ph.D. thesis, Colorado School of Mines, Dept. of Geophysics, Golden, Colorado, USA.
- Rüger, A., 1997, P-wave reflection coefficients for transversely isotropic models with vertical and horizontal axis of symmetry. *Geophysics*, 62(3), 713-722.
- Rüger, A., 1998, Variation of P-wave reflectivity with offset and azimuth in anisotropic media. *Geophysics*, 63(3), 935-947.
- Shuey, R. T., 1985, A simplification of the Zoeppritz equations. *Geophysics*, 50(4), 609-614.
- Thomsen, L., 1986, Weak elastic anisotropy. *Geophysics*, 51, 1954–1966.
- Thomsen, L., 1995, Elastic anisotropy due to aligned cracks in porous rock. *Geophysical Prospecting*, 43(6), 805-829.
- Tsvankin, I., 1997, Anisotropic parameters and P-wave velocity for orthorhombic media. *Geophysics*, 62(4), 1292-1309.
- Vavryčuk, V., and I. Pšenčík, 1998, PP-wave reflection coefficients in weakly anisotropic elastic media: *Geophysics*, 63, 2129–2141.
- Zoeppritz, K., 1919,. On the reflection and propagation of seismic waves at discontinuities. *Erdbebenwellen VII B*, 66-84.